Aeroacoustic Characteristics of a Strut-braced High-lift Device

Luke Bowen,* Hasan Kamliya Jawahar Jr.† and Mahdi Azarpeyvand‡
University of Bristol, Bristol, United Kingdom, BS8 1TR

The aerodynamic and aeroacoustic performance of a strut-based high-lift device were evaluated and demonstrated for six different strut models. The primary objective of the study was to investigate the impact of strut modifications on reducing noise levels. The aerodynamic characteristics are presented with the aid of surface pressure distribution on the airfoil that remained consistent across all the tested configurations. The aeroacoustic results are presented as the near-field surface pressure fluctuations and far-field noise measurements to attain a profound comprehension of the noise generation mechanism. Although the Albatros strut exhibited the greatest reduction in tonal noise, the directivity pattern and the overall sound pressure level of the radiated noise demonstrated that the medium height strut configuration can achieve noise reduction of up to 8 dB. The near-field unsteady surface pressure measurements are suggestive of harmonic oscillations. The coherence studies carried out have shown a decrease in the tonal coherence for the small height strut configuration while the velocity field measurements performed in the wake of the high-lift device show no significant variation in flow patterns between different strut configurations.

I. Introduction

Targets set by the European Commission's Flight Path 2050 (FP2050) require future commercial aircraft to reduce CO_2, NO_x and noise emissions by 75%, 95% and 65%, respectively [1]. In order to achieve these necessary targets, aircraft architecture will have to undergo significant changes to increase their aerodynamic efficiency and reduce their noise signature. Besides engine noise, the second-largest contributor to aircraft noise is the airframe. The changes to the design of the airframe have the potential to improve the overall aerodynamic performance of the aircraft, reduce its fuel consumption, and also reduce the overall noise signature of the vehicle. One such concept is to significantly increase the wing span, and thus the wing aspect ratio, and to include a strut/truss system to reduce bending moment on the wing structure from aerodynamic loading. Two concepts based on this revolutionary planform are the ONERA ALBATROS concept [2] and NASA's SUGAR volt concept [3] that has recently been designated the newest x-plane [4].

A strut-braced wing (SBW) is a specific type of truss-braced wing (TBW). The only distinction between SBW and TBW lies in the number of structural members supporting the wing [5]. For instance, a TBW with no supporting members corresponds to a traditional monoplane configuration, while a TBW with a single member is classified as an SBW. The concept of a truss-braced wing for transonic transport was first proposed in the 1960's by Pfenninger [6]. Chakraborty et al. [7], performed a comparative assessment of SBW and TBW configurations to optimize the latter for minimum fuel consumption. A large multidimensional design space featuring design variables across major aircraft design disciplines, including TBW configurations with one and two juries and various span limits, as well as various laminar wing design options in conjunction with lift augmentation system options, were explored as part of this study and candidate designs with desired attributes were produced.

Potential performance benefits of SBW include improved aerodynamics through increased wing span (i.e. wing aspect ratio) without significant weight gain, in contrast to traditional cantilever wings. Ongoing research activities, including ONERA's ALBATROS project, have explored the potential use of SBW configurations in civil transport aircraft [8]. Previous studies suggest that SBW designs could offer benefits such as lower gross weight, reduced empty weight, and fuel consumption [9]. Lamer et al. [10] conducted a study aimed at developing high aspect ratio wings with the potential for enhanced performance and decreased drag. The study involved testing several wing designs, and the results confirmed that the implementation of high aspect ratio strut-braced wings can result in the reduction of the induced drag. As outlined above, due to the obvious aerodynamic and fuel consumption benefits of strut-braced wing

*Research Associate, Department of Aerospace Engineering
†Research Associate, Department of Aerospace Engineering
‡Professor of Aerodynamics and Aeroacoustics, Department of Aerospace Engineering

configurations, investigations are currently underway to study other properties of such systems, such as their noise signature. For instance, McConnell [11] performed simulations using NASA's Aircraft NOise Prediction Program (ANOPP) to predict noise from an aircraft that featured transonic truss-braced wings and evaluate the noise reduction advantages of the design. Predictions from multiple flight paths during both takeoff and approach conditions indicated a considerable noise reduction. Another investigation undertaken by Leifsson [12] focused on the development of an aircraft through Multidisciplinary Design Optimization (MDO) while considering noise constraints. The study explored the feasibility of employing SBW configurations with fuselage-mounted engines, and the results demonstrated that the noise levels produced were similar to that of a conventional reference aircraft, with a minor reduction in some cases. However, it was noted that vortex shedding at the intersections of the struts could potentially generate additional noise.

It has been demonstrated that the noise generated by the slats and flaps during the approach phase of flight can contribute up to 3 to 5 EPNdB of the vehicle overall noise[13]. The deployment of flaps and slats in high-lift devices leads to the formation of a complex flow characterized by flow separation and shear-layer instability in both the slat region and in close proximity to the flap side edges. These complex flow dynamics give rise to the generation of a strong noise that can propagate to the far-field and contribute to the overall airframe noise levels [14]. Previous research has established that the noise radiated from conventional slat and wing configurations encompasses both broadband and tonal noise components. The slat cavity tonal peaks, often referred to as the Rossiter modes [15, 16], are associated with the acoustic feedback mechanism, excited due to slat cove shear layer and vortex shedding at the slat trailing edge, as demonstrated by Khorrami et al. [17], Terracol et al. [18] and several other studies [19–35]. It has also been shown that there exists a quadratic interaction between these peaks [28–31, 36]. Recent studies have also identified a spectral hump in the low-frequency range [18, 30, 32–35]. According to Pascioni et al. [30], the low-frequency broadband hump is associated with the slat cove bulk-oscillation that occurs due to the flapping of the slat cusp shear layer. Recent studies of slat noise have also revealed that the shear layer caused by the separation over the slat cusp is subject to flapping that is closely related to, and can modify the cavity tonal noise frequency [37]. Moreover, Souza et al. [38] and Wang et al. [39] explored the vortex dynamics within a slat cove, establishing a connection between the vortex structures and the narrowband peaks observed in the flow spectra. The complexity of vortex dynamics in the vicinity of a slat cove, as indicated by Wang et al. [39, 40], may originate from investigations carried out at lower Reynolds numbers. Despite the fact that the experiments are conducted at lower Reynolds numbers, Wang et al. [39, 40] suggest that insights gained from examining slat cove dynamics at lower Reynolds numbers can enhance the understanding of these dynamics at higher Reynolds numbers.

Given the significant contribution of the airframe noise to the overall noise signature of aircraft, various technologies, including both passive and active flow control methods, have been developed and tested in an attempt to suppress the noise generation mechanisms at source. These technologies include the use of porous materials [41–45], morphing structures [46, 47], finlets [48, 49], and serrations [50–54]. While a wide range of technologies have been developed for reducing noise from conventional high-lift devices, the noise generation mechanisms of SBW configurations and ways to reduce their noise signature have remained largely unexplored.

U-HARWARD (Ultra High Aspect Ratio Wing Advanced Research and Designs) is an EU Clean-Sky2 project that encompasses the detailed aerodynamic, aeroacoustic, and aeroelastic design and analysis of the SBW concepts [55]. As a part of the U-HARWARD project, the investigation of the aeroacoustic performance of a strut-braced wing in a take-off and landing configuration was deemed important as the strut system is likely to change the pressure field around the high lift device, and thus change the noise generation mechanisms from the wing slat and flap. Also, the strut-wing junction and the strut wake field interaction with the flap are likely to introduce new sources of noise, which are not properly investigated or understood. In this study, we have performed a large experimental aerodynamic and aeroacoustic campaign for a range of SBW configurations and have assessed the noise signature of such new configurations.

The paper is laid out such that the experimental set-up including the aeroacoustic facility, the 30P30N high lift device test rig, strut configurations design, and the measurement approach are outlined in section II. The results and discussion, which includes verification of the steady pressure coefficient without the struts, in impact of the strut on pressure coefficient, the near- and far-field noise measurements of the 30P30N airfoil with multiple strut configurations, coherence analysis and detailed velocity measurements are presented in section III and conclusions are made in section III.F.

Retracted airfoil chord	c	0.35 m
Slat chord	c_s	0.15c
Main-element chord	c_{me}	0.83c
Flap chord	c_f	0.3c
Slat deflection angle	δ_s	30°
Flap deflection angle	δ_f	30°
Slat gap	g_s	2.95%
Flap gap	g_f	1.27%
Slat overhang	o_s	−2.5%
Flap overhang	o_f	0.25%
Tripping device thickness	t_t	0.6 mm
Tripping device streamwise length	t_l	3 mm

Table 1 Geometrical parameters of the 30P30N high-lift airfoil.

II. Experimental setup

A. Wind tunnel

The experiments were performed in the University of Bristol Aeroacoustic Facility, which is a closed-circuit, open-jet anechoic wind tunnel. The acoustic chamber has physical dimensions of 6.7 m x 4.0 m x 3.3 m and is anechoic down to 160Hz [56, 57]. The contraction nozzle outlet has physical dimensions of 500 mm in width and 775 mm in height, which allows for a steady operation from 5 m/s to 45 m/s and a normal turbulence intensity level below 0.2% [56, 57]. A schematic of the experimental setup for the aeroacoustic measurements of the high-lift device is depicted in Fig. 1(a). The distance between the nozzle exit and the slat leading edge is 1.43 chord length. The high-lift device was mounted upside down, as shown in the photograph of the wind tunnel (see Fig. 1(b)), to evaluate the noise that would be transmitted to the ground. The image shows the high-lift device mounted with the Albatros strut.

B. Airfoil model

The airfoil model employed in the present study is a three-element MDA 30P30N high-lift airfoil with a retracted chord length of $c = 0.35$ m. The precise geometric characteristics of the airfoil are specified in Table 1 and illustrated in Fig. 2. The airfoil model was fabricated from 6000 series aluminum using computer-aided CNC machining techniques. The model was mounted to the wind tunnel nozzle using side plates, which were equipped with a turntable mechanism to allow for the adjustment of the angle of attack. To maintain two-dimensional flow within the slat cove and main-element cove regions, the brackets connecting the slat and flap to the main element were located at each spanwise end of the model, beyond the flow field. To induce turbulent flow over the slat cusp, a zig-zag flow-tripping device was placed upstream of the slat cusp on the slat suction side. The Cartesian coordinate system (x, y, z) was established with the origin at the leading edge of the main element, as shown in Figs. 2 and 3. The airfoil model was equipped with 103 static pressure taps located at the mid-span of the 30P30N airfoil to accurately measure the pressure distribution across the model. Static pressure measurements were obtained using three Chell MicroDaq-32 pressure acquisition systems and were sampled for 16 s at a frequency of 312 Hz. The airfoil model was also instrumented with miniature Knowles FG-3329-P07 pressure transducers for the measurement of unsteady surface pressure. The microphones are mounted under the skin of the airfoil behind 0.4 mm holes, which avoid pressure attenuation at high frequencies. Prior to the measurements, all microphones were calibrated in phase and magnitude to a reference GRAS 40PL microphone, further details of this procedure are found in the literature [58]. The data was sampled at 2^{16} Hz for 16 seconds with a National Instruments PXIe-4499 module.

C. Strut configurations

As part of the H2020 U-HARWARD project, a range of new strut-braced wing configurations were designed and fabricated for tests at different flight operating conditions [55]. This included subsonic take-off and landing, as well as transonic cruise conditions. A range of strut designs were proposed to withstand the different load and aeroelastic

No.	Slat Upper (mm)	Slat Lower (mm)	Main-Element Upper (mm)	Main-Element Lower (mm)	Flap Upper (mm)	Flap Lower (mm)
1	-4.6	-3.9	15.1	17.6	305.7	305.3
2	-8.1	-5.3	17.3	23.8	309.2	307.0
3	-12.1	-6.9	23.5	29.7	312.6	309.1
4	-17.3	-11.3	29.4	36.9	315.6	311.5
5	-18.7	-12.7	36.8	44.2	318.3	316.4
6	-21.	-13.8	44.1	58.8	323.6	321.4
7	-23.6	-14.6	58.8	73.2	328.4	326.4
8	-25.7	-14.8	72.6	102.4	333.2	331.3
9	-27.7		102.4	131.5	336.3	337.8
10	-29.0		131.5	160.6	340.9	342.4
11	-29.2		160.6	189.7	350.6	346.8
12	-26.4		189.7	204.3	359.7	355.5
13	-22.6		204.1	218.8	369.1	364.0
14	-18.5		218.8	233.3	374.4	372.5
15	-13.08		233.3	244.9	379.4	378.3
16			251.4	244.9	383.6	383.1
17			266.6	248.8	385.3	388.1
18			279.1	268.1	389.3	391.1
19			286.8	281.8	391.9	393.4
20			292.7	290.7	394.8	
21				292.8		

Table 2 Static pressure tap locations along the mid-span of the 30P30N airfoil.

	No.	x (mm)	z (mm)
Main-Element	M1-1	22.4	12
	M1-2	22.4	15.6
	M1-3	22.4	23.4
	M1-4	22.4	36.4
	M1-5	22.4	54.6
Flap	F1-1	308.8	12
	F1-2	308.8	15.6
	F1-3	308.8	23.4
	F1-4	308.8	36.4
	F1-5	308.8	54.6
	F2-1	349.3	12
	F2-2	349.3	15.6
	F2-3	349.3	23.4
	F2-4	349.3	36.4
	F2-5	349.3	54.6

Table 3 Microphone locations on the 30P30N airfoil as depicted in Fig. 4(d).

conditions which dictated the strut geometry for the aeroacoustic investigation. Each strut featured a fixed chord length of 0.1 m and was set at a 9° inclination angle relative to the airfoil surface, as shown in Fig. 3. The strut's cross-section adopted a symmetric NACA0012 profile. Furthermore, the strut chord was designed to align with the chord line of the 30P30N airfoil. The two chosen parameters to vary for this study were the height of the vertical section of the strut, and the mounting location of each strut. Three different strut heights were considered, namely, the small height, the medium height, and the Albatros strut, which was inspired by the ONERA Albatros wing design [2]. For the second parameter, two chordwise mounting positions for the strut-wing junction were investigated, namely the mid-chord position and the trailing edge position of the main element. The effect of the strut on the high-lift device was analyzed in terms of its aerodynamic and acoustic properties using six different strut models, as illustrated in Fig. 3. The struts were manufactured using solid laser sintering (SLS) techniques from polyamide material in a single part. All strut elements were designed to mount to the mid-span of the model parallel to the airfoil, with the root of the strut attached to the wind tunnel side-plate. To ensure a turbulent boundary layer over the struts and mitigate any laminar flow instability noise (i.e. T-S waves), a zig-zag tripping device was applied to both sides of the strut element at 10% of the strut chord.

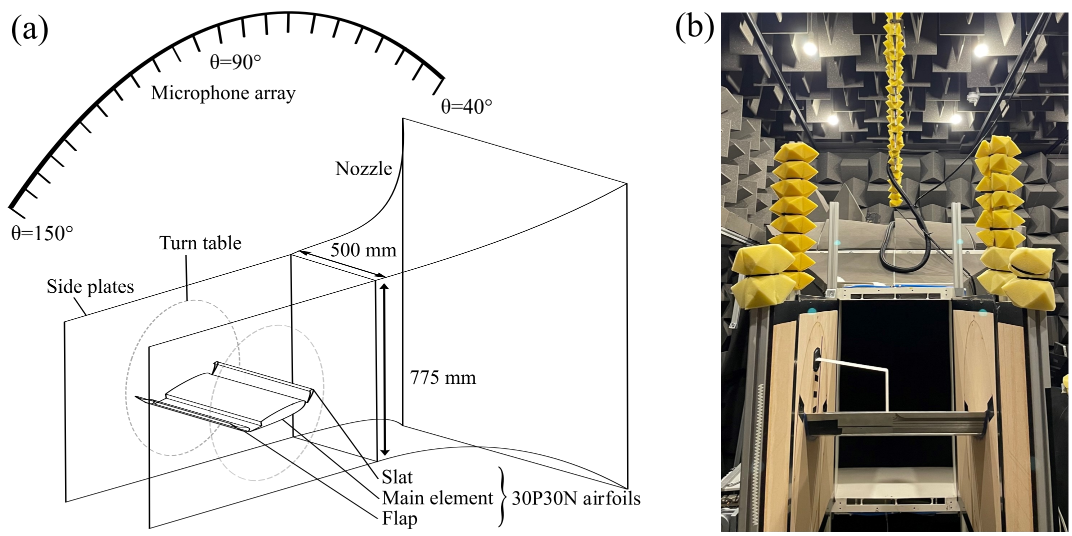

Fig. 1 Schematic and an image of the experimental setup describing 30P30N airfoil mounting to wind tunnel nozzle.

D. Far-field measurement

The acoustic performance of the high-lift device fitted with the struts was evaluated by mounting the airfoil model upside-down in the wind tunnel, positioning the slat with a direct line of sight to the far-field microphone array located at the top of the tunnel. The array consists of 23 microphones arranged at 5° increments between polar angles of $\theta = 40°$ and $\theta = 150°$ to allow for directivity measurements. The arc was located 1.75 m above the airfoil model, and the microphone at $\theta = 90°$ was located directly above the slat element of the airfoil. The microphones on the arc were 1/4 inch GRAS 40PL microphones, which exhibit a flat frequency response for a large dynamic range of 10 Hz and 20, 000 Hz. All microphones were calibrated using a GRAS 42AA pistonphone calibrator prior to the experiments.

E. Hot-wire anemometry setup

The flow properties in the wake of the strut-wing configuration were characterized by the use of Constant Temperature Anemometry Hot-wire. A Dantec 55P63 right-angled miniature X-wire probe was used to characterize the two components of the flow deflection in the airfoil wake. The probe was operated using a Dantec Streamline Pro system with a CTA91C10 module, using a National Instruments PXIe-4499 module mounted in a National Instruments PXIe-1026Q chassis for data acquisition. The data were simultaneously sampled at a rate of 2^{15} Hz for a duration of 16 s. The X-wire probe was calibrated daily using a Dantec 54H10 calibrator for both velocity and yaw angles between −40° and 40°.

The hot-wire measurement locations around the slat region and in the flap wake region are illustrated in Fig. 4. Both

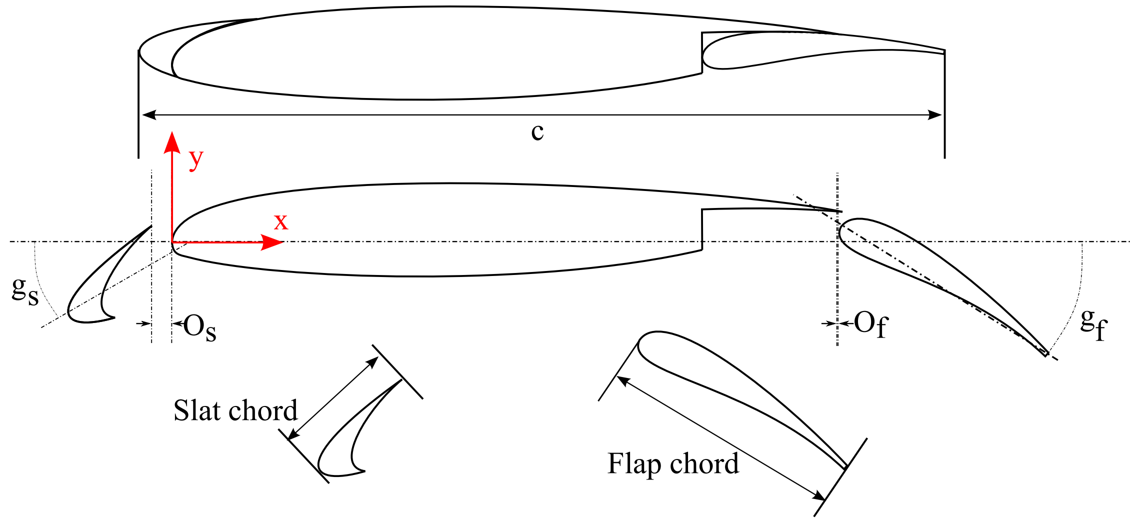

Fig. 2 Geometric definitions of 30P30N airfoil.

Measurement	x (mm)	y (mm)	z (mm)
Slat (Position 1)	-24.8	-62.1 to -12.1	100,-100
Slat (Position 2)	-17.4	-43.4 to -13.4	100,-100
Slat (Position 3)	-11.7	-43.5 to -2.5	100,-100
Flap (Position 1)	366.5	-354.2 to -54.2	100,-100
Flap (Position 2)	433.5	-354.2 to -54.2	100,-100

Table 4 Velocity measurement locations around the 30P30N airfoil where the datum point in on the leading edge of the main element. Only the range of measurements has been provided in the y-direction for brevity.

crosswise and streamwise measurement locations on the slat and the flap are shown in Figs. 4(a) and 4(b). Figure 4(c) shows the three spanwise locations on the airfoil at which measurements were performed. The first location was situated in the vertical plane of the junction between the strut and the airfoil. The other two locations were positioned on either side of this plane, with a distance of $z/c = 0.285$ from the mid-span of the high-lift device. This enabled the distinction between the strut-side and the non-strut side regions on the airfoil. The coordinate datum adopted during the study has been illustrated in Fig. 4(d).

III. Results

The outcomes of the experimental investigation are presented in this section, focused on characterizing the effect of each strut configuration on the noise generated by the high-lift device. The study first assesses the mean pressure field around the airfoil at multiple angles of attack and the effect of each strut on the pressure field. The far-field noise characteristics of the high-lift device and each strut are then presented, followed by the assessment of the velocity measurements in the wake of the airfoil.

A. Pressure coefficient

To analyze the influence of each strut configuration on the mean pressure field in the center-span of the 30P30N airfoil, the mean wall-pressure coefficient is presented. The results are presented for the mean-flow velocity of $U_\infty = 30$ m/s, which corresponds to a retracted chord-based Reynolds number of $Re = 7.1 \times 10^5$. The non-dimensional mean pressure coefficient (C_p) is analyzed for the slat element and all three elements of the high-lift device. The results are presented in separate subplots, with the Baseline 30P30N configuration shown first to highlight its sensitivity to the change in angle of attack. The effect of each strut configuration on C_p is then examined at the angle of attack of $\alpha = 14°$.

Li et al. [32] demonstrated that the results of the 30P30N high-lift airfoil obtained from testing in an open jet

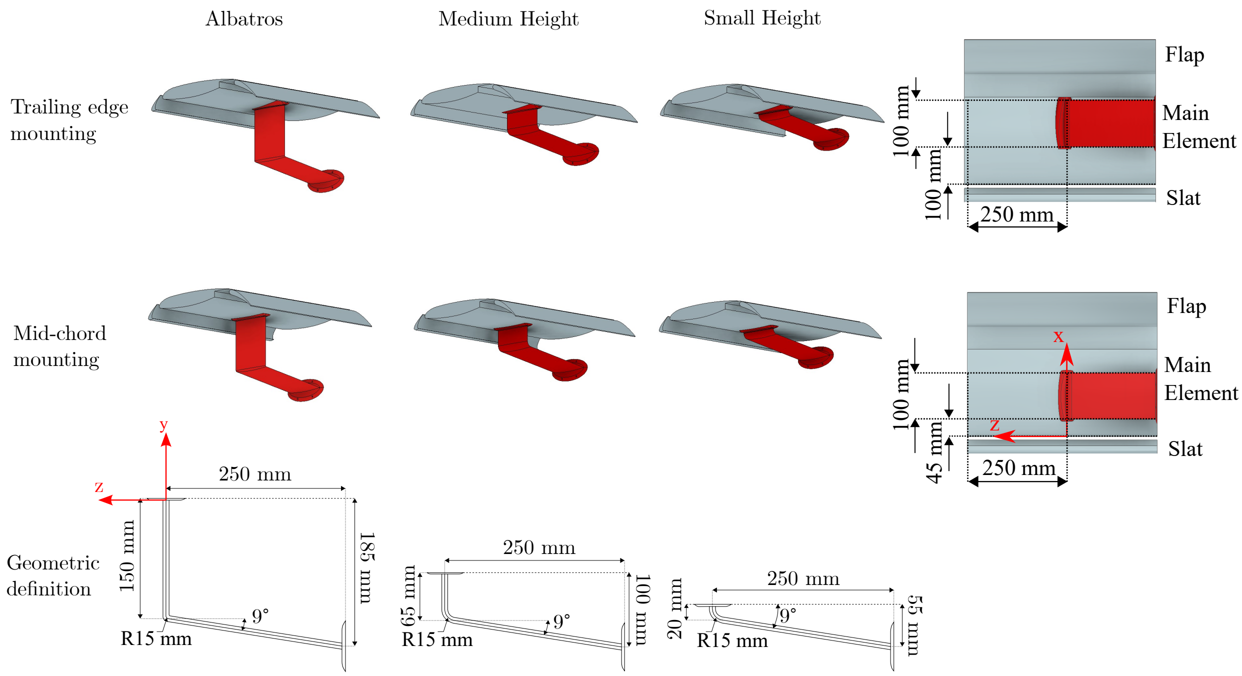

Fig. 3 Schematic of the six different strut configurations fitted on the high-lift device.

wind tunnel diverge from those obtained in a closed test section wind tunnel. This distinction is a widely recognized phenomenon, where the difference between the geometric angle of attack and the freestream angle of attack arises from the wind tunnel sidewall interference. Previous studies conducted at the University of Bristol aeroacoustic facility [59] have recorded an 8.5° difference between the geometric and freestream angle of attack for the 30P30N high-lift configuration. Li et al. [32] and Manoha and Pott-Pollenske [60] also reported similar discrepancies in their research on high-lift devices.

Figure 5 shows the pressure coefficient distribution for the 30P30N Baseline configuration for the angles of attack ranging from $\alpha = 8°$ to 18° with an increment of 2°. The changes in C_p over the slat and the complete airfoil have been presented in Figs. 5 (a) and (b), respectively. The results of the study indicate that as the angle of attack increases the C_p distribution over the slat and main elements also increases, possibly due to increased loading on these components at increasing angles of attack. This could also be attributed to the higher flow velocity in the slat gap which leads to an increase in the suction peak on the main element as the angle of attack is increased. Previous experimental results have also been included to Fig. 5(b) for accuracy verification against the standard Baseline 30P30N airfoil pressure coefficient results collected in this study. It is of note that the aforementioned correction of 8.5° difference is confirmed in Fig. 5(b), where the results of this experimental campaign are compared with previous experimental results from the D5 aeroacoustic wind tunnel (D5-WT) of Li et al. [32] and the closed-section Low Turbulence Wind Tunnel (LTWT) experiments from Jawahar et al. [59].

Figure 6 presents a comparison of the C_p results for the Baseline configuration and various strut configurations, evaluated at an angle of attack of 14°. The figure illustrates the effect of the height and chordwise mounting location of the strut on the C_p distribution. The results for the slat and the complete airfoil are shown in Figs. 6(a) and (b), respectively. Six strut configurations were tested, including three mid-chord mounted and three trailing-edge mounted strut configurations. Three strut heights were tested, namely, small height, medium height, and Albatros strut, which were mounted both in the middle of the chord and at the trailing edge. The results demonstrate that modifications to the strut configuration have a subtle effect on the suction peak on the slat. The suction peak exhibits a marginal increase on the slat, as indicated by the results presented in Figs. 6(a) and (b) However, no substantial deviations are observed in the pressure coefficient (C_P) distribution on the airfoil with differing strut modifications.

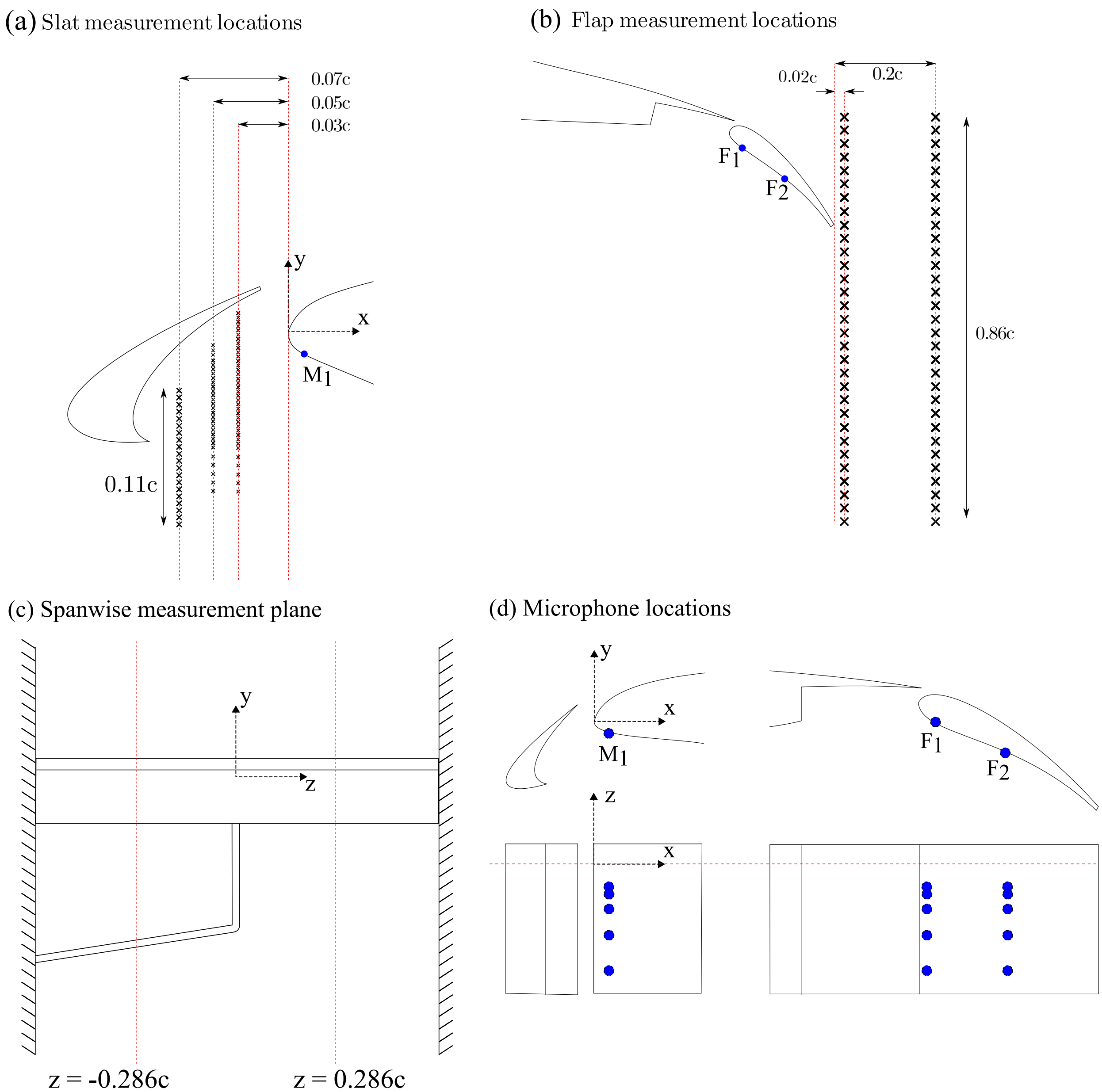

Fig. 4 Velocity measurement locations for the (a) slat region, (b) the flap wake, (c) spanwise planes for each measurement and (d) the coordinate datum.

B. Far-field noise

In the current subsection, a comprehensive evaluation of the far-field noise generated by the 30P30N airfoil is carried out. The primary objective is to examine the effect of varied strut arrangements on the magnitude of the far-field noise. The far-field noise is quantified using the power spectral density (PSD) level, which is measured at a microphone placed directly above the slat element on the lower surface of the airfoil, at an angle of $\theta = 90°$. The PSD is computed as $PSD = 10 \cdot \log_{10}(\phi_{pp}/p_{ref}^2)$, where ϕ_{pp} represents the Power Spectral Density of the pressure fluctuations and p_{ref} is the reference pressure of 20μPa. The PSD results are presented in terms of the Strouhal number, defined as $St_s = fc_s/U_\infty$. The data obtained from this measurement serves as a means to assess the performance of various strut configurations in terms of far-field noise emissions.

The far-field measurements for the Baseline configuration compared with the Albatros strut configurations have been presented in Fig. 7(a) and a close-up view of the tonal peak is shown in Fig. 7(b). The results for the Baseline airfoil

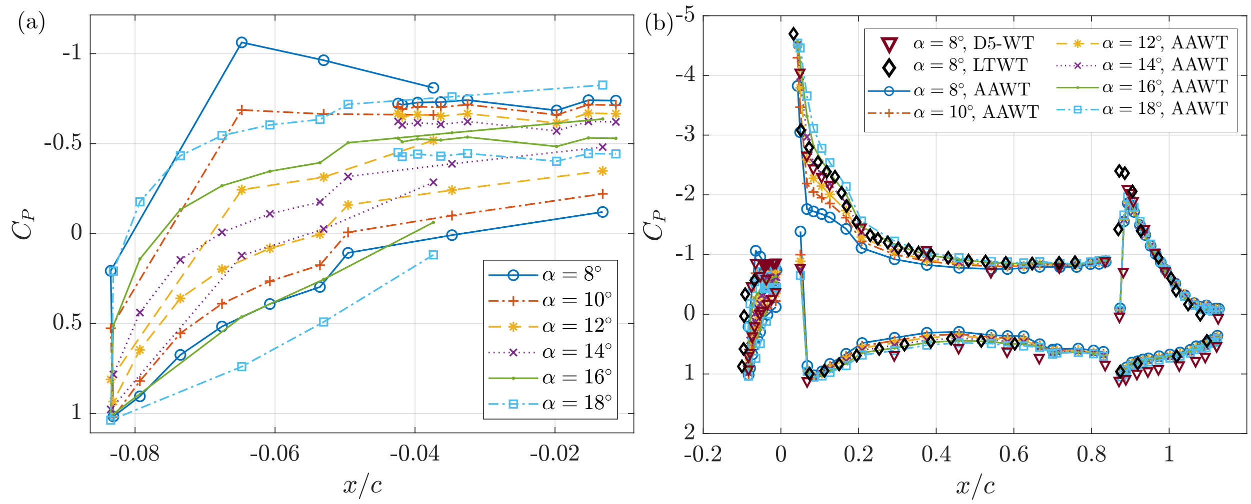

Fig. 5 Pressure coefficient distribution for the 30P30N airfoil at multiple angles of attack between $8° < \alpha < 18°$ where (a) is a close-up of the slat and (b) is the full airfoil and has comparison with previous experimental data as D5-WT [32] and LTWT [59].

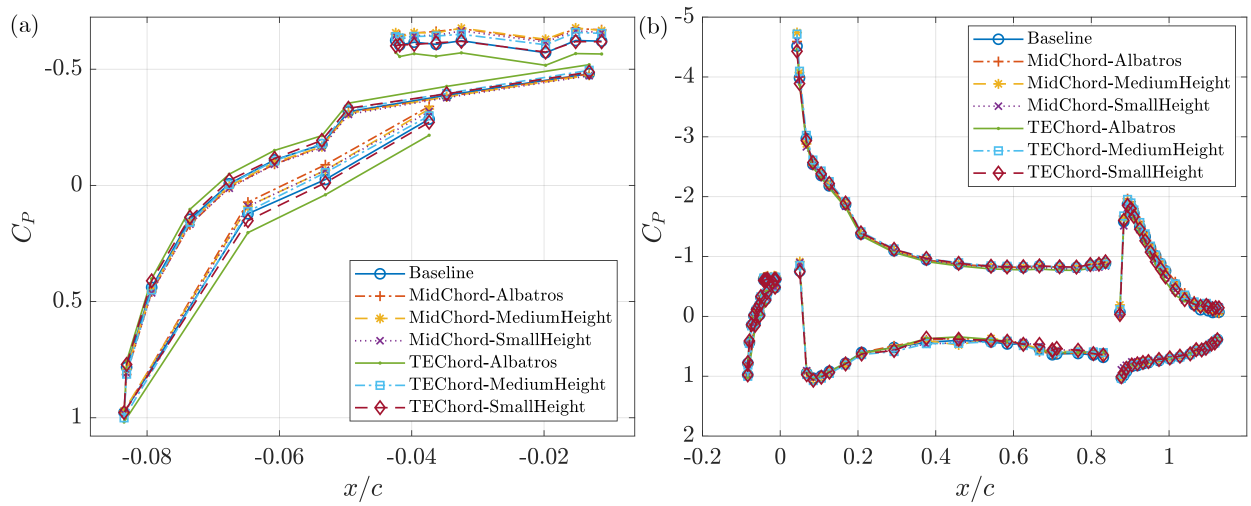

Fig. 6 Pressure coefficient distribution for the 30P30N airfoil Baseline and all the strut configurations at angle of attack $\alpha = 14°$ (a) close up of the slat and (b) full airfoil.

reveal the presence of fundamental frequency and its harmonics which is a typical noise signature of high-lift devices. This is primarily attributed to the flow-acoustic coupling phenomenon called the Rossiter modes. Rossiter modes are a set of discrete frequencies that can be observed in cavities and arise due to the oscillations that are influenced by the acoustic feedback from the shear layer impingement region [15]. The first acoustic mode is due to the slat cavity resonance and the higher modes can be described as the summation of multiples of the lower modes, as described in Table 4 of Jawahar et al. [59]. Previous study demonstrates the link between the slat shedding frequency mode, the harmonics of the shedding frequency as two other modes, and further combinations of these modes [59, 61].

The characteristic tonal peaks with varying intensities are also observed for the Albatros strut configurations. The tonal peak observed at $St_s = 1.5$ displays the highest intensity for both the Baseline and the tested strut configurations. Furthermore, it is observed that the trailing edge mounted Albatros strut configuration, results in a substantial decrease in tonal noise levels of up to 8 dB coupled with a reduction in low-frequency broadband noise. The tonal peaks exhibit a harmonic nature, with peaks appearing at regular intervals, a consequence of the flow-acoustic coupling phenomenon that leads to resonance [47].

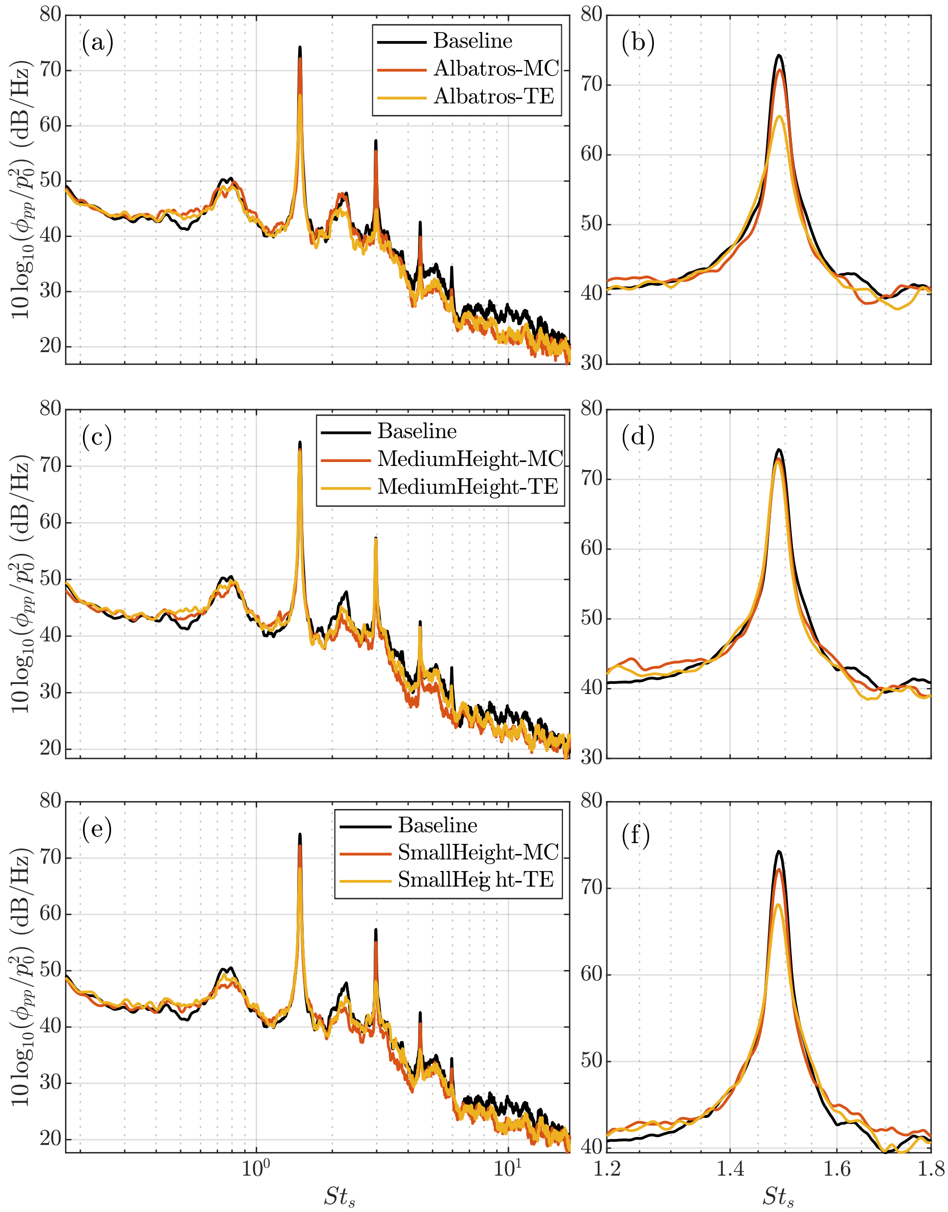

Fig. 7 Far-field noise of the Baseline 30P30N observed at polar angle $\theta = 90°$, compared with (a) and (b) the Albatros strut mounted at the mid-chord and trailing edge locations, (c) and (d) the medium height strut mounted at the mid-chord and trailing edge locations, (e) and (f) the small height strut mounted at the mid-chord and trailing edge locations.

Comparisons between the Baseline and medium height strut configurations are presented in Figs. 7 (c) and (d). The far-field spectra display a similar pattern, characterized by multiple tonal peaks for the Albatros and small height strut configurations. However, the tonal peaks, with varying intensities, demonstrate a minimal reduction in noise for the medium height when compared to the Baseline configuration. When comparing the Baseline with the small height configuration (see Figs. 7 (e) and (f)), a slight reduction in the tonal peak is observed. The tonal peak reduction is more pronounced than that observed for the medium height configurations, although less than the reduction seen in the Albatros configurations. Overall, the Albatros strut configurations exhibit the maximum reduction in the tonal noise levels when compared to both the medium and small height configurations.

The directivity of the radiated noise is presented in terms of the overall sound pressure level. The results are presented here for the polar angle range of $40° < \theta < 130°$. The data for angles larger than $\theta = 130°$ are not presented due to direct flow interaction with the microphones and noise contamination. The overall sound pressure level is calculated as,

$$OASPL = 10 \cdot \log_{10} \left[\frac{\int \phi_{pp}(f) df}{p_{ref}^2} \right], \tag{1}$$

integrating the energy spectrum with respect to frequency, between 160 Hz< f <20,000 Hz. The results for the Albatros strut configuration have been presented in Fig. 8(a) while those for the medium height and small height strut have been shown in Figs. 8(b) and (c), respectively. The directivity plot for the Baseline configuration shows an increase in OASPL at the polar angle of $\theta = 55°$ seen as a peak in the plot. A similar trend is also observed for all the strut configurations. However, the strut configurations show a substantial noise reduction of up to 5 dB compared to the Baseline at this position as seen in Fig. 8. Mounting the strut at the trailing edge in the Albatros configuration yields more significant noise reduction when compared to the results of the mid-chord mounting location. In contrast, the medium height configurations shown in Fig.8(b) demonstrate better performance when mounted at mid-chord position. The results for the small height configurations (see Fig.8(c)) show the minimal difference between the trailing edge and mid-chord mounting positions. Interestingly, the most notable noise reduction can be observed for the medium-height strut configuration mounted at the mid-chord position, with a reduction of up to 8 dB. However, when considering the total noise reduction over the directivity angles that are presented, the Albatros strut in the trailing edge configuration demonstrates the most consistent noise reduction.

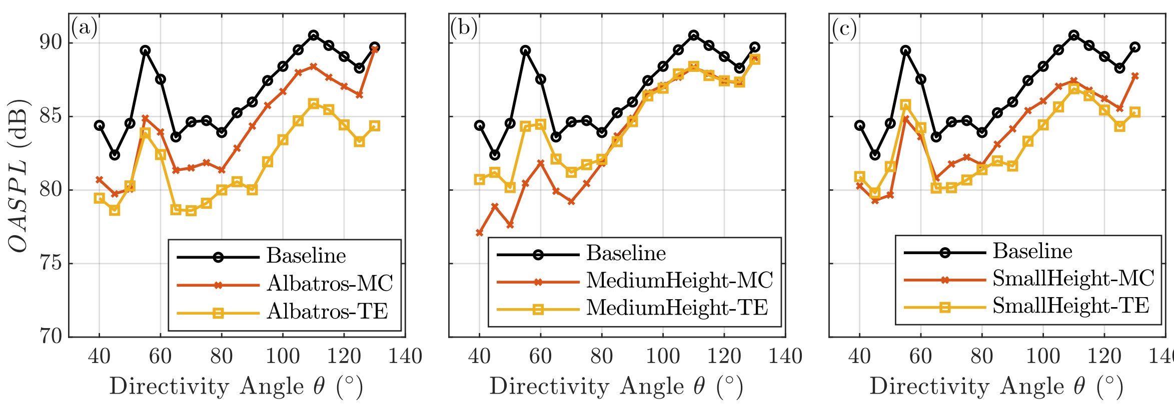

Fig. 8 Directivity of the OASPL of the Baseline 30P30N airfoil compared to each strut configuration at mid-chord and trailing edge mounting where (a) Albatros height strut, (b) medium height strut and (c) small height strut.

C. Near-field measurements

In order to achieve a comprehensive understanding of the noise generation mechanism, a series of near-field unsteady surface pressure measurements were conducted. The SPL of the surface pressure fluctuations was determined on the main element and the flap along the centerline of the 30P30N airfoil and presented in comparison with the Albatros and small height strut configurations. SPL is plotted against the dimensionless Strouhal number. Figures. 9(a) and (b) present the pressure fluctuations measured at the location $x/c = 0.06$ on the leading edge of the main element at the slat vicinity. As can be observed from the results, multiple tonal peaks were seen for the Baseline case due to the Rossiter modes and the feedback mechanism previously discussed (see sec. III.B). The surface pressure fluctuation results demonstrate the presence of multiple tonal peaks in the data which correspond to the tonal peak observed in the far-field noise data, see Fig. 7. The tonal peak behavior in the surface pressure fluctuation further reinforces the suggestion of the harmonic nature of the flow over the slat as the tonal peaks observed in the surface pressure fluctuation also correspond to the tonal peaks observed in the far-field. The relationship between tonal response exhibited by the near-field and far-field pressure fluctuations reinforces the modal behavior of the slat noise that can be predicted by a simplified Rossiter mode equation [59, 62]. Furthermore, in corroboration with the far-field noise results, the near-field surface pressure results for the Albatros and the small height strut configurations reveal a substantial reduction in the tonal component of the fundamental peak and its harmonics.

The pressure fluctuations measured at the location $x/c = 0.88$ on the leading edge of the flap have been shown in

Figs. 9(c) and (d). The results reveal the presence of the fundamental tonal peak and its harmonics at this location for the Baseline case, but not for the Albatros and small height strut configurations. The acoustic energy of the tonal noise observed in the results of the Baseline case is strong enough to propagate to the flap, yet the results for the Albatros and small height configurations exhibit very little tonal behavior at this streamwise location. Additionally, the spectra for the tested configurations demonstrate an increase in the broadband nature, potentially due to the flow from the wake of the strut. This increase in the broadband nature is more pronounced for the Albatros configuration than for the small height strut, due to increased wake flow from a larger area.

Figures. 9(e) and (f) show the results for the tested configurations at a further downstream position at location $x/c = 0.99$ at the mid-chord of the flap. The tonal component observed in the Baseline case exhibits a much more pronounced presence due to the superior line of sight for acoustic propagation towards the slat. Moreover, the Albatros and small height strut configurations are associated with an increase in low-frequency broadband noise, which is attributed to the wake flow from the strut.

D. Coherence

In this section, the magnitude-squared coherence between surface pressure fluctuations at three chordwise locations and three far-field locations is presented, considering the frequency, the position of the microphones, and the polar angle of far-field observers. The magnitude-squared coherence is calculated as

$$\gamma^2_{p_i p_j}(f) = \frac{\phi^2_{p_i p_j}(f)}{\phi_{p_i p_i}(f)\phi_{p_j p_j}(f)}, \tag{2}$$

where $\gamma^2_{p'_i p'_j}(f)$ is the magnitude-squared coherence calculated between near-field and far-field pressure fluctuations, and $\phi_{p'_i p'_j}$ denotes the cross-power spectral density between the near-field and far-field microphones i and j, respectively. The three microphones M_1, F_1 and F_2 are positioned at the chordwise locations $x/c = 0.06$, $x/c = 0.88$ and $x/c = 0.99$, respectively. The far-field microphone locations are considered at the polar angles $\theta = 55°$, $90°$ and $120°$. The near-to-far-field coherence results observed at these locations have been presented in Fig. 10 in terms of Strouhal number.

The coherence results between position M_1 on the main element of the airfoil and the polar angles $\theta = 55°$, $90°$, and $120°$ (see Figs. 10(a), (b), and (c)) indicate the highest levels of coherence at all angles for both the Baseline and tested strut configurations. Additionally, the results reveal a highly directional tonal component. Figures 10 (d), (e), and (f) present the coherence levels between position F_1 at $x/c = 0.88$ on the flap leading edge and all three polar angles, revealing a high degree of coherence for the Baseline configuration. However, the results indicate a substantial decrease in tonal coherence for the small-height strut configuration. The Albatros configuration, on the other hand, exhibited no tonal coherence. Notably, the near-field SPL spectra demonstrated an increase in low-frequency broadband noise, while the near-to-far-field coherence did not exhibit any such variation.

Figures 10 (g), (h), and (i) show coherence between the microphone position F_2 ($x/c = 0.99$) close to the flap trailing-edge and all the three polar angles ($\theta = 55°$, $90°$, and $120°$). The results for the Baseline configuration show high coherence for the tonal components. Also, the plots show high coherence for low-frequency hump for the Baseline case at all three polar angles. However, at 90° the coherence for this low-frequency hump is higher than that observed at position 55°. Additionally, this hump is not coherent for the Albatros and small height configurations. Furthermore, the coherence of the tonal component for the small height configuration is significantly reduced in comparison to the Baseline. Whereas, the Albatros configuration shows lesser coherence than both the Baseline and small height configuration for the tonal component. Overall, it can be seen from the results that the coherence at positions F_1 and F_2 is not as substantial as the Baseline configuration from the flap region for both the strut cases.

The spanwise coherence of the surface pressure fluctuations, measured using embedded microphones inside the wing ($M1$, $F1$ and $F2$), is studied to shed light on the coherent flow structures passing over the airfoil, and how the addition of a strut influences the coherence. The coherence of pressure fluctuations for three spanwise separations ($\gamma^2_{p_i p_j}(f, \Delta z)$) is shown in Fig. 11 for three chordwise locations where $M1$ is located at $x/c = 0.06$, $F1$ is located at $x/c = 0.88$ and $F2$ is located at $x/c = 0.99$. Here, Δz is the separation distance between the surface pressure microphones in the spanwise direction. The coherence is calculated in the same manner as the near-field to far-field coherence using equation III.D, as a function of $\Delta z/c$ The results obtained by the microphone M_1 at chordwise location $x/c = 0.06$ are shown in Figs. 11 (a), (b) and (c) for $\Delta z/c = 0.077$, $\Delta z/c = 0.46$ and $\Delta z/c = 0.81$, respectively. The results for all the tested configurations show very high levels of coherence for the smallest lateral spacing $\Delta z/c = 0.077$ at all frequencies. This is expected as the small separation distance captures the pressure fluctuations from the same flow structure. As

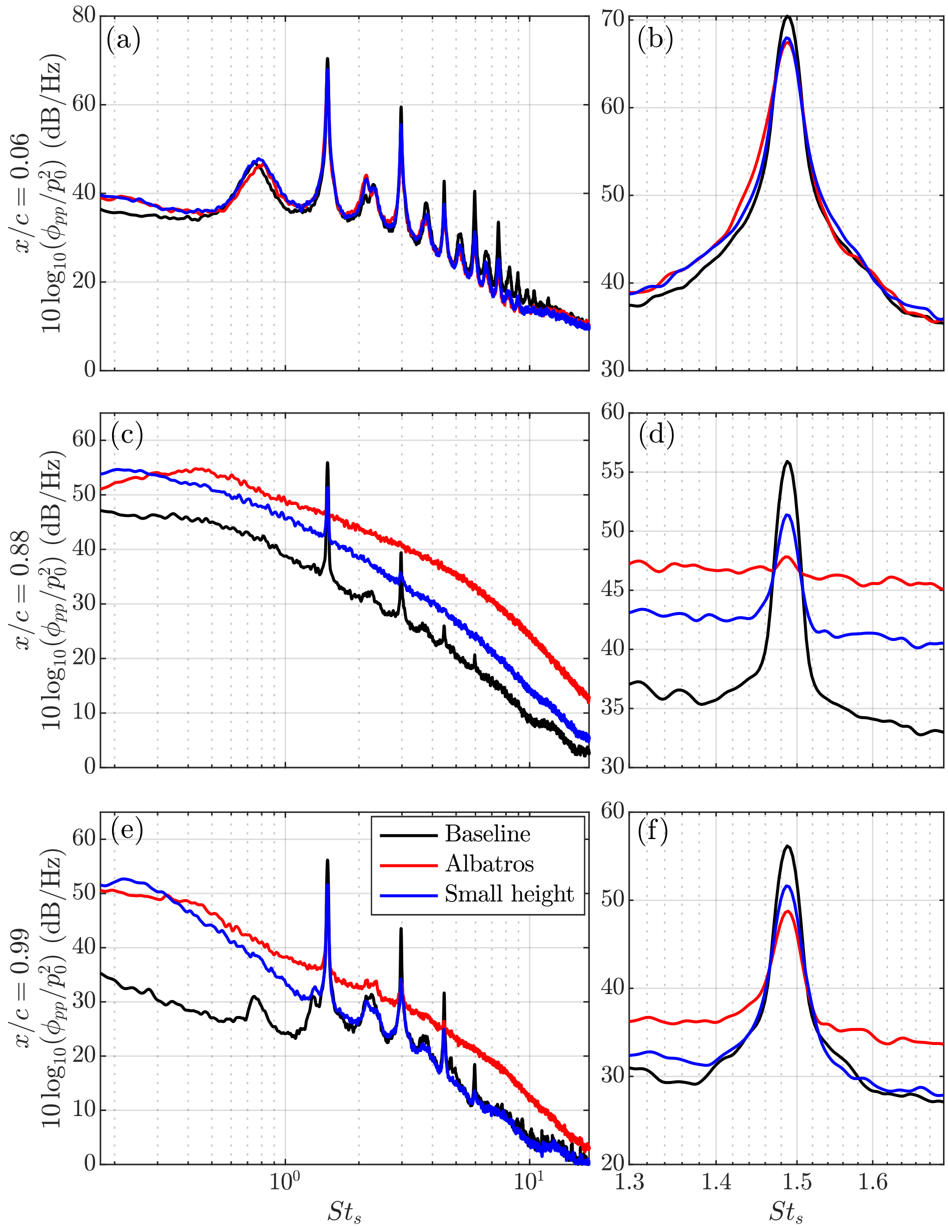

Fig. 9 Power spectral density of the surface pressure fluctuations against Strouhal number along the center line $z/c = 0.03$, for (a) and (b) on the pressure side of the 30P30N main element, $M1$ at $x/c = 0.02$, for (c) and (d) on the pressure side of the 30P30N flap element $F1$ at $x/c = 0.88$ and for (e) and (f) on the pressure side of the 30P30N flap element $F2$ at $x/c = 0.99$.

the spanwise separation increases to $\Delta z/c = 0.46$, the broadband component reduces with the reduction in coherence in the low- and high-frequency regimes with tonal peaks. This could be attributed to more complex flow structures that are not captured by both sensors. Furthermore, for the largest separation at the spanwise location $\Delta z/c = 0.88$, further reduction in the coherence levels is observed in the low- and high-frequency regime since the flow structures are different at each location. The reduction of the broadband component of the spectra at low- and high-frequencies results in the tonal element of the coherence becoming much more prominent. The tonal element of the spanwise coherence is characteristic of both the near- and far-field results presented in Sec. III.B and III.C.

The spanwise coherence at position F_1 located at the leading edge of the flap at $x/c = 0.88$ are presented in Figs. 11 (d), (e) and (f). The results obtained at the nearest spanwise separation of $\Delta z/c = 0.077$ reveal a rise in the

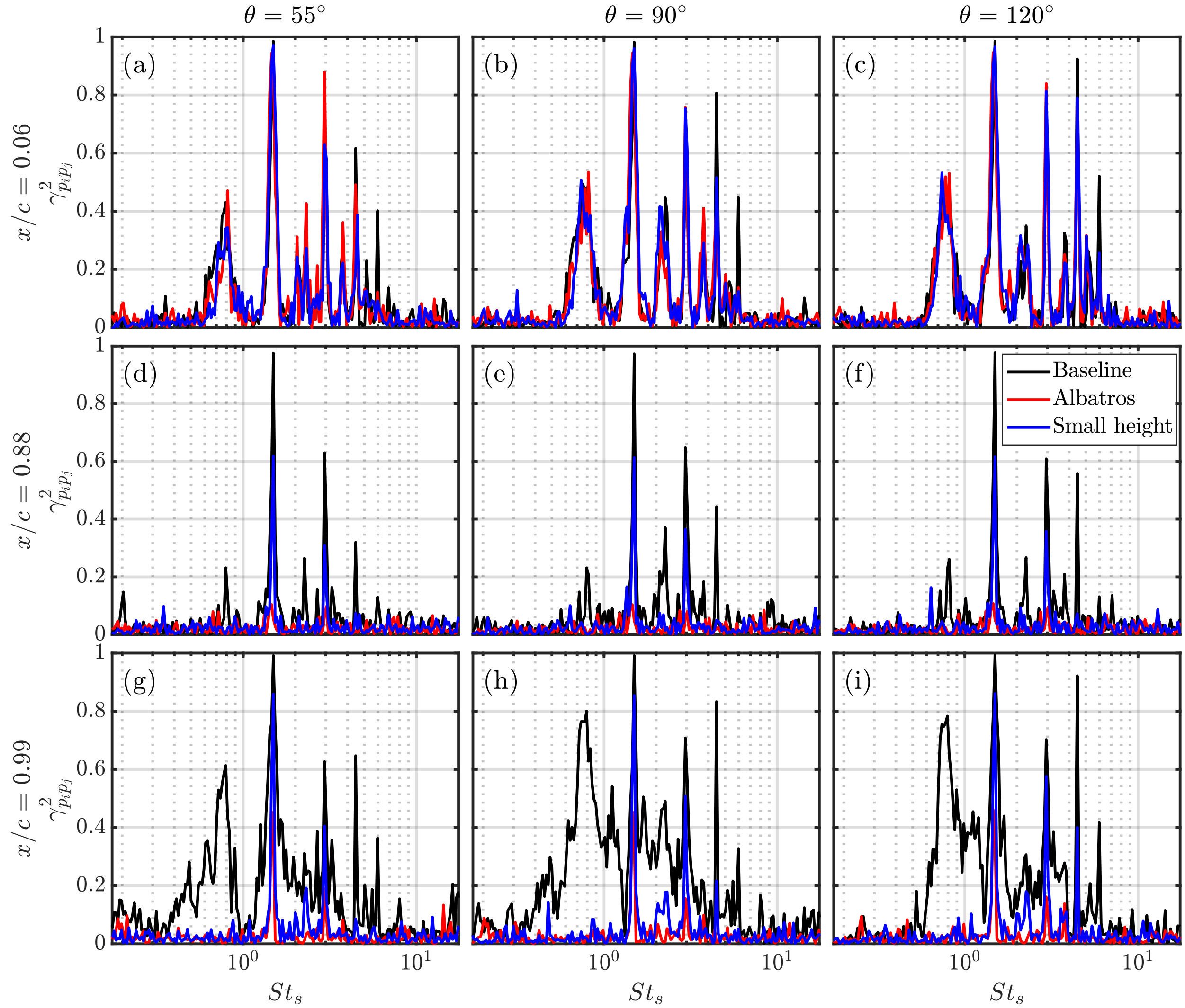

Fig. 10 Magnitude square coherence between the surface pressure fluctuations to the pressure fluctuations at the far-field observers against Strouhal number, for three chordwise locations where $M1$ is on the main element (x/c = 0.06), and $F1$ and $F2$ are located on the flap (at x/c = 0.88 and x/c = 0.99, respectively), to three polar angle of far-field observers $\theta = 55°$, $\theta = 90°$ and $\theta = 120°$.

tonal component in the high-frequency range for the Baseline, along with a significant broad hump. As the spanwise separation increases, the tonal component for the Baseline reduces in the low- and high-frequency range, as shown in Figure 11(e) and (f). Conversely, the small height strut configuration exhibits high coherence at low frequency, which decreases notably in the high-frequency range for the nearest spanwise separation. Similarly, the Albatros strut configuration follows the same pattern, but its coherence levels at low-frequency are lower than those of the small height strut configuration. At locations, $\Delta z/c = 0.46$ and $\Delta z/c = 0.81$, an increase in the spanwise separation shows almost no coherence for the small height and Albatros configurations, with a minor amount of tonal behavior, primarily attributed to the slat tones.

The measurements acquired by the microphone F_2 at $x/c = 0.99$ have been presented in Figs. 11 (g), (h) and (i). At the closest spanwise separation, the Baseline case shows little coherence at low-frequency and higher coherence as the frequency further increases. Conversely, the Albatros and small height configurations show high coherence at low-frequency and reduced levels at high frequency, possibly due to the strut wake interaction with the flap. Both the tested cases retain the tonal behavior in the results presented. It is important to note the observed tones at the flap trailing edge could be attributed to their acoustic behavior. The small height configuration shows higher coherence than

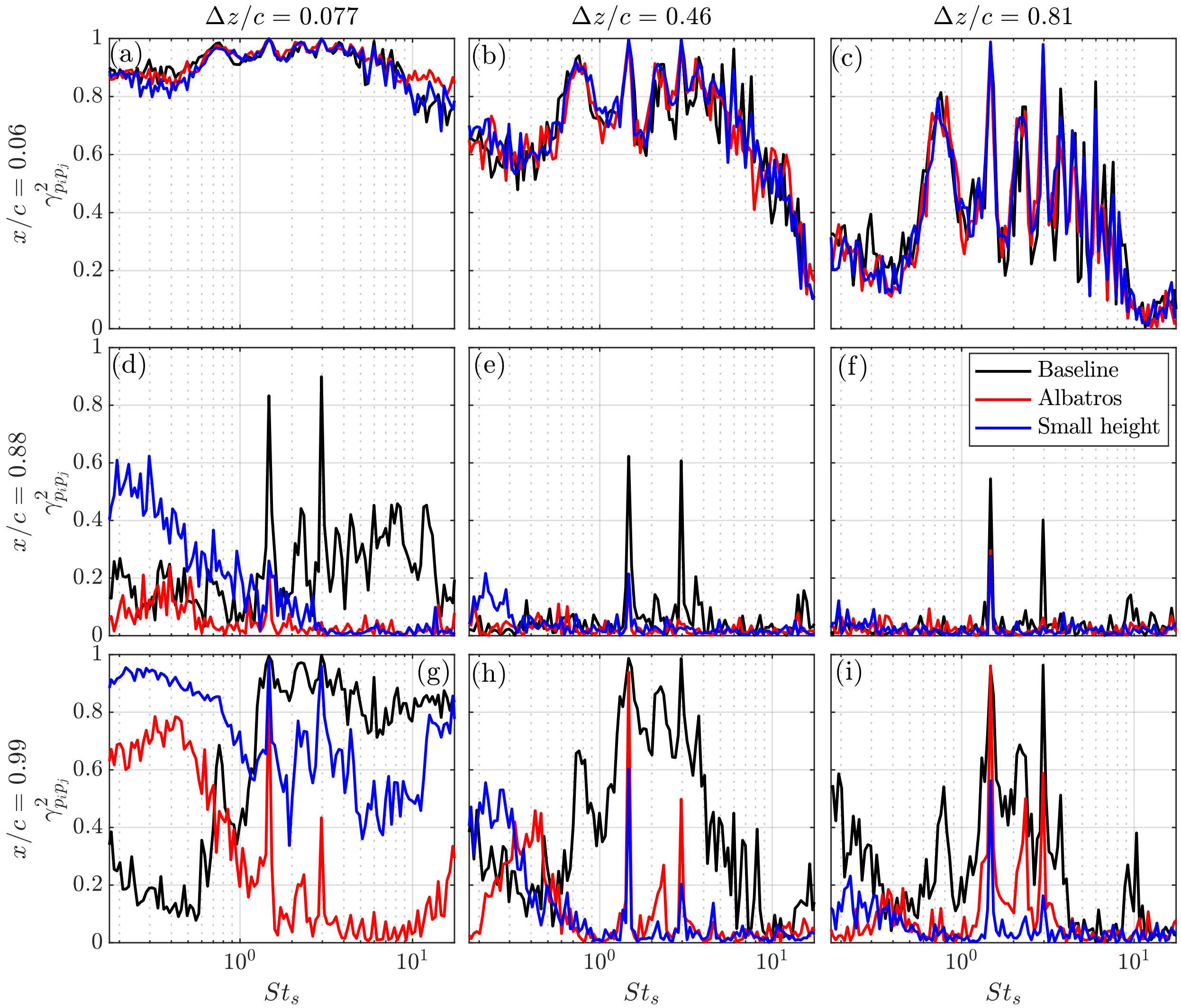

Fig. 11 Magnitude square coherence between the surface pressure fluctuations for three different spanwise separations $\Delta z/c = 0.077$, $\Delta z/c = 0.46$ and $\Delta z/c = 0.81$, for three chordwise locations where $M1$ is on the main element ($x/c = 0.06$), and $F1$ and $F2$ are located on the flap (at $x/c = 0.88$ and $x/c = 0.99$, respectively).

the Albatros strut. With further increase in the separation, at location $\Delta z/c = 0.46$, a high coherence is observed for the Baseline case in the mid-frequency region while the two tested struts show negligible coherence at high frequency. However, both the strut configurations show very high levels of coherence for the tonal component at these positions. A similar trend can be seen in the results for the location $\Delta z/c = 0.81$ for both the broadband and tonal components.

.

E. Velocity measurement

In this section, the characteristics of the velocity field near the 30P30N airfoil are investigated for the Baseline as well as two distinct strut configurations: the small height trailing edge mounting and the Albatros trailing edge mounting. Measurements are conducted by traversing a CTA X-wire hot-wire probe along the y-axis at multiple downstream locations and two spanwise positions ($z/c = 0.286$ and $z/c = -0.286$) for each strut configuration. Both the slat and flap regions are examined, taking into account the non-strut side and strut side, see Fig. 4.

Figure 12 shows the mean streamwise and crosswise velocities ($\overline{U}$ and $\overline{V}$) obtained at three distinct locations ($x/c = -0.07, -0.05, -0.03$) in the vicinity of the slat for the Baseline, Albatros, and small height TE configurations. Figures 12(a)-(f) depict the $\overline{U}$ and $\overline{V}$ values measured on the non-strut side, while Figs. 12(g)-(l) represent the

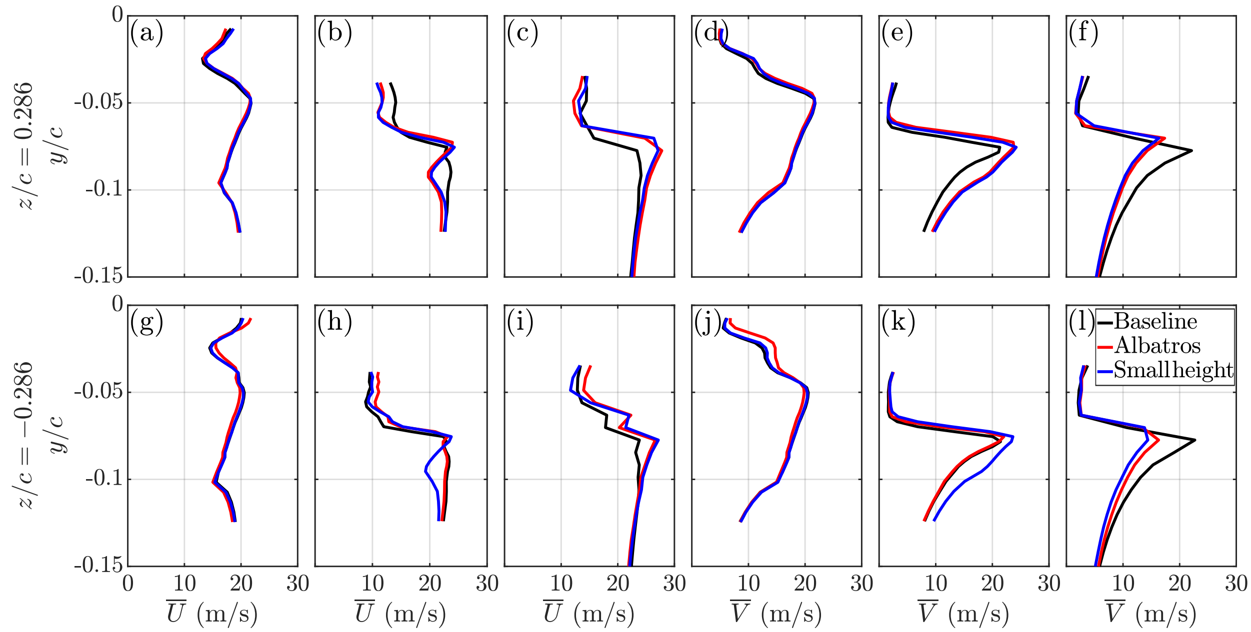

Fig. 12 Mean flow velocity measured at three locations in the region of the slat element for the Baseline, Albatros TE and small height TE configurations, where velocity measurements are presented for $\overline{U}$ ((a)-(c) and (g)-(i)) and $\overline{V}$ ((d)-(f) and (j)-(l)), at two spanwise locations of z/c = 0.286 (a)-(f) and z/c = −0.286 (g)-(l) relating to the non-strut-side and strut-side, respectively.

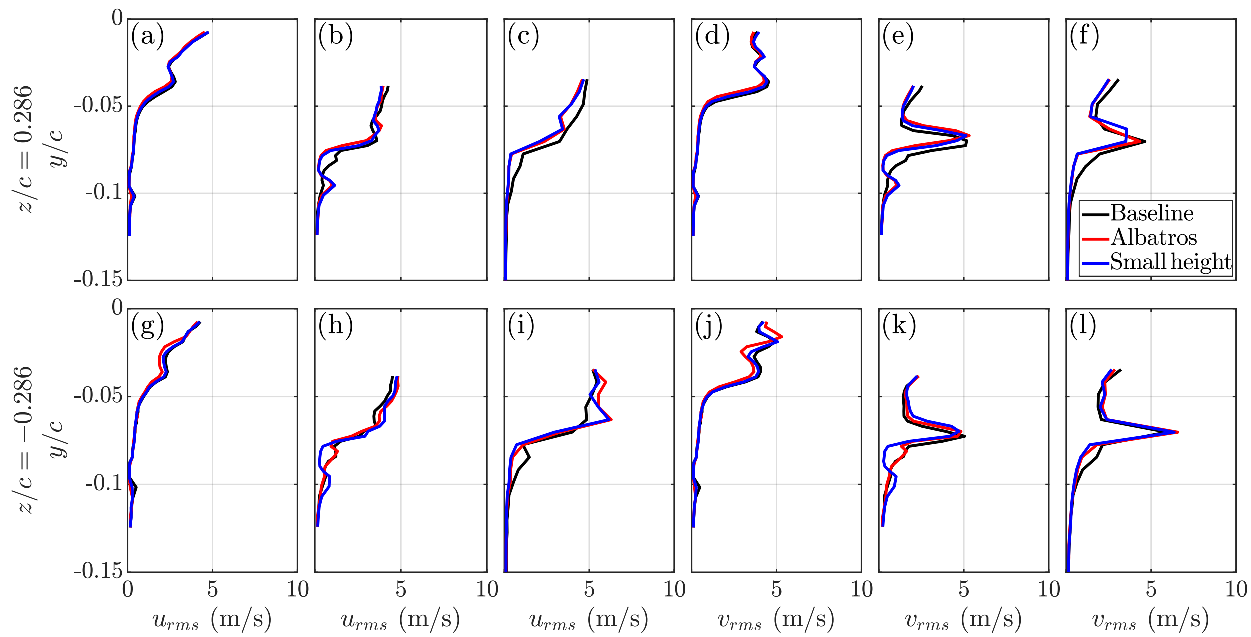

Fig. 13 Root-mean-square of velocity fluctuations measured at three locations in the region of the slat element for the Baseline, Albatros TE and small height TE configurations, where velocity measurements are presented for u_{rms} ((a)-(c) and (g)-(i)) and v_{rms} ((d)-(f) and (j)-(l)), at two spanwise locations of z/c = 0.286 (a)-(f) and z/c = −0.286 (g)-(l) relating to the non-strut-side and strut-side, respectively.

corresponding measurements on the strut side. At $x/c = -0.07$, the velocities shown in Figs. 12(a), (g), (d), and (j) exhibit no notable differences among all tested cases, with the exception of the $\overline{V}$ value measured on the strut side

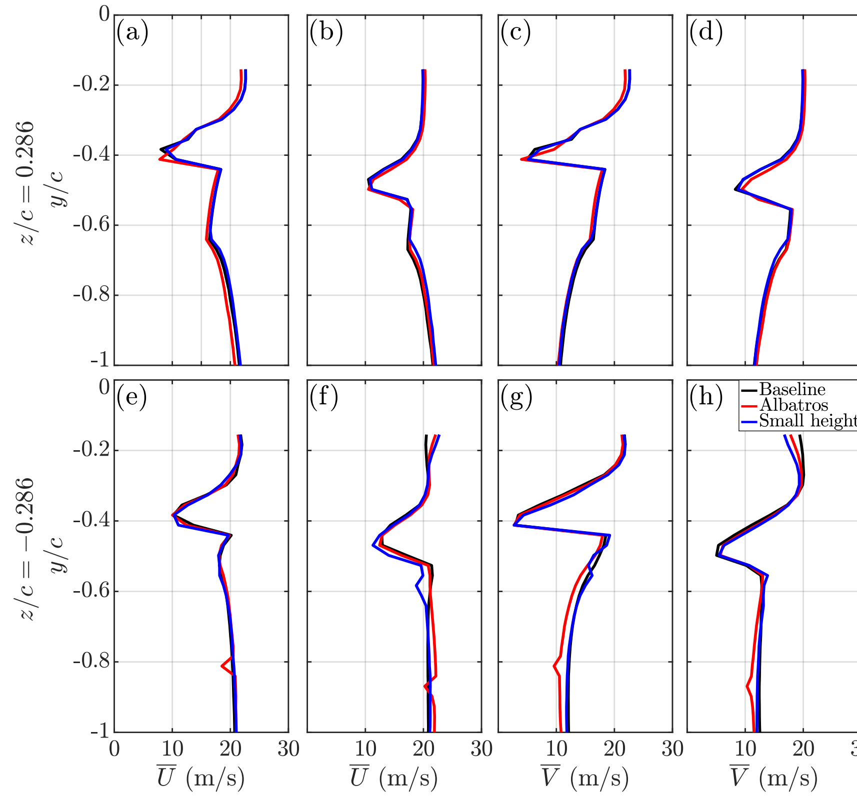

Fig. 14 Mean flow velocity measured at two locations in the flap wake for the Baseline, Albatros TE and small height TE configurations, where velocity measurements are presented for $\overline{U}$ ((a)-(b) and (e)-(f)) and $\overline{V}$ ((c)-(d) and (g)-(h)), at two spanwise locations of $z/c = 0.286$ (a)-(d) and $z/c = -0.286$ (e)-(h) relating to the non-strut-side and strut-side, respectively.

(Fig. 12(j)), which displays variations for the Albatros strut configuration at $y/c > -0.05$. For the next downstream location, $x/c = -0.05$, the $\overline{U}$ exhibits an S-shaped pattern in wake measurements, indicative of vortex presence, likely resulting from vortex shedding at the slat cusp. Notably, the strut configurations reveal more significant alterations compared to the Baseline on the non-strut side (Fig. 12(b)). On the strut side, however, the Albatros configuration causes minimal disruption to the flow relative to the small height configuration. The crosswise velocity $\overline{V}$ at $x/c = -0.05$ (Fig. 12) follows a similar trend to that of the streamwise velocity concerning disparities among the cases. At the third measurement location, $x/c = -0.03$, a clear distinction emerges between the streamwise and crosswise velocity outcomes for each strut configuration when compared with the Baseline. In the range of $-0.07 < y/c < 0.1$, the primary variation between the strut configurations and the Baseline involves an increase in the streamwise velocity and a reduction in the crosswise velocity.

The global impact of the strut on the mean flow across the slat appears to be minimal, as no major differences in flow behavior are observed on either the strut or non-strut side. Furthermore, the most pronounced changes occur in the $\overline{V}$ values on both the non-strut and strut sides, where discrepancies arise between the Baseline and the evaluated strut cases. The most significant alterations are evident in the measured velocities at the third location, $x/c = -0.03$, as presented in Figs. 12(c), (i), (f), and (l), with the most considerable changes observed in the measured $\overline{V}$ values. Interestingly, the $\overline{V}$ values on both the non-strut and strut sides are relatively similar, even though they were anticipated to be different.

The root-mean-square of velocity fluctuations measured at all three locations in the slat region ($x/c = -0.07, -0.05, -0.03$) are presented in Fig. 13. The measurements on the non-strut side are presented in Figs. 13(a)-(f), while the corresponding values on the strut side are shown in Figs. 13(g)-(l). These results identify areas of high flow unsteadiness and potential shear flow development due to separation over the slat cusp. Velocity measurements for u_{rms} and v_{rms}

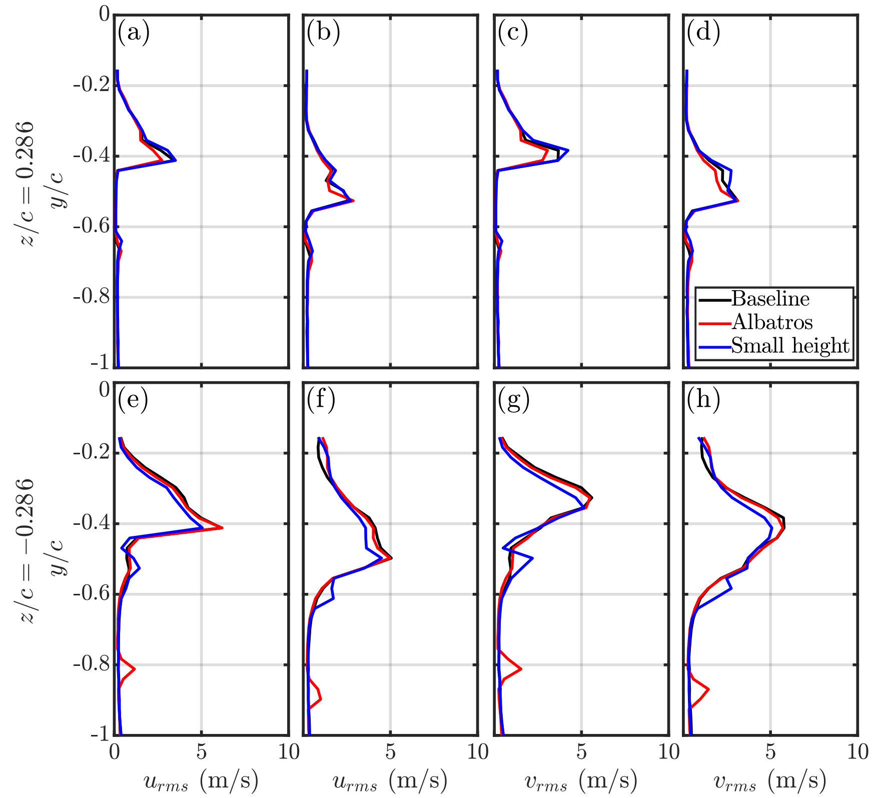

Fig. 15 Root-mean-square of velocity fluctuations measured at two locations in the flap wake for the Baseline, Albatros TE and small height TE configurations, where velocity measurements are presented for u_{rms} ((a)-(b) and (e)-(f)) and v_{rms} ((c)-(d) and (g)-(h)), at two spanwise locations of $z/c = 0.286$ (a)-(d) and $z/c = -0.286$ (e)-(h) relating to the non-strut-side and strut-side, respectively.

reveal that the root-mean-square velocities are relatively similar between the Baseline and strut configurations. However, a slight increase in u_{rms} and v_{rms} is observed at $z/x = -0.286$ for both strut configurations, indicating an overall rise in flow unsteadiness on the strut side of the airfoil span. In summary, the root-mean-square velocity findings suggest that the strut exerts no significant influence on the unsteady flow over the slat.

Mean flow velocities measured at two locations in the flap wake for the Baseline, Albatros trailing edge (TE), and small height TE configurations are presented in Fig. 14. The streamwise velocity measurements, $\overline{U}$, at two spanwise locations of $z/c = 0.286$ and $z/c = -0.286$, are shown in Figs. 14(a), (b), (e), and (f), while the crosswise velocity measurements, $\overline{V}$, are shown in Figs. 14(c), (d), (g), and (h). The subplots in Figs. 14(a)-(d) present the measurements for the non-strut side, and Figs. 14(e)-(h) display the results for the strut side. The measurements on the strut side reveal uniformity in the values, with no significant variations observed. However, an examination of the flow field indicates the presence of wake remnants on the strut side for both the mean streamwise velocity ($\overline{U}$) and the mean crosswise velocity ($\overline{V}$). Notably, this observation is made at two distinct locations due to the existence of two different strut heights. The small velocity deficit observed can be attributed to the thin profile of the strut, which minimizes the impact of the wake. A comparison of the crosswise velocity of the Albatros configuration to that of the small height and Baseline cases reveals a reduction in the former. This decrease in mean velocity in the crosswise direction suggests less deflection of the flow on the strut side in the Albatros case.

The root-mean-square of the velocity fluctuations for both streamwise and crosswise velocities, measured at two locations in the flap wake for the Baseline, Albatros trailing edge (TE), and small height TE configurations are shown in Fig. 15. Figures 15(a)-(d) represent the non-strut side, while Figs. 15(e)-(h) illustrate the strut side. The results reveal that the non-strut side exhibits similar characteristics, with minimal reductions in u_{rms} and v_{rms} for the Albatros configuration when compared to the Baseline and small height TE configurations. Conversely, the strut side demonstrates the impact of the strut's wake, as evidenced by an increase in the level of root-mean-square velocity fluctuations at locations $y/c = -0.5, -0.8$. Furthermore, a decrease in the level of root-mean-square velocity fluctuations is observed for the small height strut configuration. A deviation from the Baseline results is also noted for the Albatros case, attributed to the previously observed reduction in vertical velocity (see Figure 14).

F. Conclusion

The aerodynamic and aeroacoustic characteristics of strut-based high-lift devices were investigated by employing six distinct strut models, encompassing three varying strut heights: small, medium, and Albatros. It was observed that the pressure coefficient distribution on the airfoil remained largely unaffected by diverse strut modifications, although a minor increase in the suction peak on the slat was detected. In far-field analysis, it was demonstrated that the Albatros strut configuration yielded the most substantial reduction in tonal noise levels when compared to the medium and small height configurations. The directivity of radiated noise, expressed in terms of OASPL, revealed that the medium-height strut configuration achieved the most noteworthy noise reduction, exhibiting up to an 8 dB reduction at the mid-chord position. Near-field unsteady surface pressure measurements indicated the existence of multiple tonal peaks, implying the presence of Rossiter modes with its harmonics. While the small height strut configuration exhibited a reduction in tonal coherence with the far-field, the Albatros configuration displayed an absence of tonal coherence. From the flow-field measurements, it was reported that from the flow-field measurements, the global impact of the strut on the mean flow across the slat was found to be minimal, with no significant differences in flow behavior observed on either side. It was suggested that the strut had no significant influence on the velocity fluctuations of the flow over the slat, based on the root-mean-square velocity fluctuation results. In the flap wake, it was revealed that the values for the strut side and wake remnants' presence were uniform, according to the measurements. The Albatros configuration showed a reduction in crosswise velocity, indicating less flow deflection compared to the small height and Baseline cases. Overall, the study provided valuable insights into the effects of strut modifications on noise reduction in aircraft.

IV. Acknowledgements

The content of this document reflects only the author's view. The European Commission and Clean Sky 2 Joint Undertaking (CS2JU) are not responsible for any use that may be made of the information it contains. The U-HARWARD Project has received funding from the Clean Sky 2 Joint Undertaking, under the European Union's Horizon 2020 research and innovation Program under Grant Agreement number: 886552 - H2020-CS2-CFP10-2019-01. The first author (L.B.) would like to acknowledge the support of EPSRC via Grant No. EP/S013024/1.

References

[1] Commission, E., for Mobility, D.-G., Transport, for Research, D.-G., and Innovation, *Flightpath 2050 – Europe's vision for aviation – Maintaining global leadership and serving society's needs*, Publications Office, 2011. https://doi.org/doi/10.2777/50266.

[2] Carrier, G., Atinault, O., Dequand, S., Hantrais-Gervois, J. L., Liauzun, C., Paluch, B., Rodde, A. M., and Toussaint, C., "Investigation of a strut-braced wing configuration for future commercial transport," *28th Congress of the International Council of the Aeronautical Sciences*, ICAS Bonn, 2012, pp. 2012–1.

[3] Bradley, M. K., and Droney, C. K., "Subsonic Ultra Green Aircraft Research: phase II–volume II–hybrid electric design exploration," *NASA CR-218704*, 2015, p. 378.

[4] Crimaldi, S., and Jorgensen, M., "Four Transformations for Sustainability, Greater Mobility, and Economic Growth," *NASA Aviation Day*, 2023.

[5] Bhatia, M., Kapania, R., van Hoek, M., and Haftka, R., "Structural design of a truss braced wing: potential and challenges," *50th AIAA/ASME/ASCE/AHS/ASC Structures, Structural Dynamics, and Materials Conference 17th AIAA/ASME/AHS Adaptive Structures Conference 11th AIAA No*, 2009, p. 2147. https://doi.org/https://doi.org/10.2514/6.2009-2147.

[6] Pfenninger, W., "Design considerations of large subsonic long range transport airplanes with low drag boundary layer suction," *Northrop Aircraft, Inc., Report NAI-54-800 (BLC-67)*, 1954.

[7] Chakraborty, I., Nam, T., Gross, J. R., Mavris, D. N., Schetz, J. A., and Kapania, R. K., "Comparative assessment of strut-braced and truss-braced wing configurations using multidisciplinary design optimization," *Journal of Aircraft*, Vol. 52, No. 6, 2015, pp. 2009–2020. https://doi.org/https://doi.org/10.2514/1.C033120.

[8] Carrier, G., Atinault, O., Dequand, S., Hantrais-Gervois, J., Liauzun, C., Paluch, B., Rodde, A., and Toussaint, C., "Investigation of a strut-braced wing configuration for future commercial transport," *28th Congress of the International Council of the Aeronautical Sciences*, ICAS Bonn, 2012, pp. 2012–1.

[9] Kulfan, R. M., and Vachal, J. D., "Wing Planform Geometry Effects on Large Subsonic Military Transport Airplanes." Tech. rep., Boeing Commercial Airplane Co, Seattle, Washington, 1978.

[10] Le Lamer, Y., Morlier, J., Benard, E., and He, P., "Aeroelastic analysis of high aspect ratio and strut-braced wings," *33th Congress of the International Council of the Aeronautical Sciences*, 2022, pp. 11–p.

[11] Mc Connell, R., "Acoustic Analysis of an Ultra-Efficient Commercial Transport Aircraft," Master's thesis, The Pennsylvania State University, 2022.

[12] Leifsson, L. T., "Multidisciplinary design optimization of low-noise transport aircraft," Ph.D. thesis, Virginia Polytechnic Institute and State University, 2006.

[13] Zhao, K., Okolo, P., Neri, E., Chen, P., Kennedy, J., and Bennett, G. J., "Noise reduction technologies for aircraft landing gear-A bibliographic review," *Progress in Aerospace Sciences*, Vol. 112, 2020, p. 100589. https://doi.org/https://doi.org/10.1016/j.paerosci.2019.100589.

[14] Guo, Y., and Joshi, M., "Noise characteristics of aircraft high lift systems," *AIAA Journal*, Vol. 41, No. 7, 2003, pp. 1247–1256. https://doi.org/https://doi.org/10.2514/2.2093.

[15] Rossiter, J., "Wind-tunnel experiments on the flow over rectangular cavities at subsonic and transonic speeds," 1964.

[16] Heller, H., and Bliss, D., "The physical mechanism of flow-induced pressure fluctuations in cavities and concepts for their suppression," *2nd Aeroacoustics conference*, 1975, p. 491. https://doi.org/https://doi.org/10.2514/6.1975-491.

[17] Khorrami, M. R., Berkman, M. E., and Choudhari, M., "Unsteady flow computations of a slat with a blunt trailing edge," *AIAA Journal*, Vol. 38, No. 11, 2000, pp. 2050–2058. https://doi.org/https://doi.org/10.2514/2.892.

[18] Terracol, M., Manoha, E., and Lemoine, B., "Investigation of the unsteady flow and noise generation in a slat cove," *AIAA Journal*, Vol. 54, No. 2, 2016, pp. 469–489. https://doi.org/https://doi.org/10.2514/1.J053479.

[19] Roger, M., and Perennes, S., "Low-frequency noise sources in two-dimensional high-lift devices," *6th Aeroacoustics Conference and Exhibit*, 2000, p. 1972. https://doi.org/https://doi.org/10.2514/6.2000-1972.

[20] Olson, S., Thomas, F., and Nelson, R., "Mechanisms of slat noise production in a 2D multi-element airfoil configuration," *7th AIAA/CEAS Aeroacoustics Conference and Exhibit*, 2001, p. 2156. https://doi.org/https://doi.org/10.2514/6.2001-2156.

[21] Khorrami, M. R., "Understanding slat noise sources," *Colloquium EUROMECH*, Vol. 449, 2003, pp. 9–12.

[22] Choudhari, M. M., and Khorrami, M. R., "Effect of three-dimensional shear-layer structures on slat cove unsteadiness," *AIAA journal*, Vol. 45, No. 9, 2007, pp. 2174–2186. https://doi.org/https://doi.org/10.2514/1.24812.

[23] Kolb, A., Faulhaber, P., Drobietz, R., and Grünewald, M., "Aeroacoustic wind tunnel measurements on a 2D high-lift configuration," *13th AIAA/CEAS Aeroacoustics Conference (28th AIAA Aeroacoustics Conference)*, 2007, p. 3447. https://doi.org/https://doi.org/10.2514/6.2007-3447.

[24] Mendoza, J., Brooks, T., and Humphreys Jr, W., "An aeroacoustic study of a leading edge slat configuration," *international Journal of Aeroacoustics*, Vol. 1, No. 3, 2002, pp. 241–274. https://doi.org/https://doi.org/10.1260/147547202320962583.

[25] Hein, S., Hohage, T., Koch, W., and Schöberl, J., "Acoustic resonances in a high-lift configuration," *Journal of Fluid Mechanics*, Vol. 582, 2007, pp. 179–202. https://doi.org/https://doi.org/10.1017/S0022112007005770.

[26] Makiya, S., Inasawa, A., and Asai, M., "Vortex shedding and noise radiation from a slat trailing edge," *AIAA journal*, Vol. 48, No. 2, 2010, pp. 502–509. https://doi.org/https://doi.org/10.1016/j.jsv.2022.117420.

[27] Murayama, M., Nakakita, K., Yamamoto, K., Ura, H., Ito, Y., and Choudhari, M. M., "Experimental study on slat noise from 30P30N three-element high-lift airfoil at JAXA hard-wall lowspeed wind tunnel," *20th AIAA/CEAS aeroacoustics conference*, 2014, p. 2080. https://doi.org/https://doi.org/10.2514/6.2018-3460.

[28] Pagani Jr, C. C., Souza, D. S., and Medeiros, M. A., “Slat noise: aeroacoustic beamforming in closed-section wind tunnel with numerical comparison,” *AIAA Journal*, Vol. 54, No. 7, 2016, pp. 2100–2115. https://doi.org/https://doi.org/10.2514/1.J054042.

[29] Pagani, C. C., Souza, D. S., and Medeiros, M. A., “Experimental investigation on the effect of slat geometrical configurations on aerodynamic noise,” *Journal of Sound and Vibration*, Vol. 394, 2017, pp. 256–279. https://doi.org/https://doi.org/10.1016/j.jsv.2017.01.013.

[30] Pascioni, K. A., and Cattafesta, L. N., “An aeroacoustic study of a leading-edge slat: Beamforming and far field estimation using near field quantities,” *Journal of Sound and Vibration*, Vol. 429, 2018, pp. 224–244. https://doi.org/https://doi.org/10.1016/j.jsv.2018.05.029.

[31] Pascioni, K. A., and Cattafesta, L. N., “Unsteady characteristics of a slat-cove flow field,” *Physical Review Fluids*, Vol. 3, No. 3, 2018, p. 034607. https://doi.org/https://doi.org/10.1103/PhysRevFluids.3.034607.

[32] Li, L., Liu, P., Guo, H., Hou, Y., Geng, X., and Wang, J., “Aeroacoustic measurement of 30P30N high-lift configuration in the test section with Kevlar cloth and perforated plate,” *Aerospace Science and Technology*, Vol. 70, 2017, pp. 590–599. https://doi.org/https://doi.org/10.1016/j.ast.2017.08.039.

[33] Li, L., Liu, P., Guo, H., Geng, X., Hou, Y., and Wang, J., “Aerodynamic and aeroacoustic experimental investigation of 30P30N high-lift configuration,” *Applied Acoustics*, Vol. 132, 2018, pp. 43–48. https://doi.org/https://doi.org/10.1016/j.apacoust.2017.11.002.

[34] Li, L., Liu, P., Xing, Y., and Guo, H., “Time-frequency analysis of acoustic signals from a high-lift configuration with two wavelet functions,” *Applied Acoustics*, Vol. 129, 2018, pp. 155–160. https://doi.org/https://doi.org/10.1016/j.apacoust.2017.07.024.

[35] Li, L., Liu, P., Xing, Y., and Guo, H., “Wavelet analysis of the far-field sound pressure signals generated from a high-lift configuration,” *AIAA Journal*, Vol. 56, No. 1, 2018, pp. 432–437. https://doi.org/https://doi.org/10.2514/1.J056160.

[36] Choudhari, M. M., and Lockard, D. P., “Assessment of slat noise predictions for 30P30N high-lift configuration from BANC-III workshop,” *21st AIAA/CEAS aeroacoustics conference*, 2015, p. 2844. https://doi.org/https://doi.org/10.2514/6.2015-2844.

[37] Wei, R., Liu, Y., Li, X., and Zhang, H., “Experimental study on the oscillation of the shear layer of the slat cavity for 30P30N Multi-Element High-Lift Airfoil,” *AIAA AVIATION 2023 Forum*, 2023. https://doi.org/10.2514/6.2023-4482.

[38] Souza, D. S., Rodríguez, D., Himeno, F. H., and Medeiros, M. A., “Dynamics of the large-scale structures and associated noise emission in airfoil slats,” *Journal of Fluid Mechanics*, Vol. 875, 2019, pp. 1004–1034. https://doi.org/https://doi.org/10.1017/jfm.2019.496.

[39] Wang, J.-S., and Wang, J.-J., “Vortex dynamics for flow around the slat cove at low Reynolds numbers,” *Journal of Fluid Mechanics*, Vol. 919, 2021, p. A27. https://doi.org/https://doi.org/10.1017/jfm.2021.385.

[40] Wang, J., Xu, Y., and Wang, J., “Slat cove dynamics of multi-element airfoil at low Reynolds number,” *Science China Technological Sciences*, Vol. 66, No. 4, 2023, pp. 1166–1179. https://doi.org/https://doi.org/10.1007/s11431-022-2308-7.

[41] Ali, S. A. S., Azarpeyvand, M., and Da Silva, C. R. I., “Trailing-edge flow and noise control using porous treatments,” *Journal of Fluid Mechanics*, Vol. 850, 2018, pp. 83–119. https://doi.org/https://doi.org/10.1017/jfm.2018.430.

[42] Ali, S. A. S., Azarpeyvand, M., and da Silva, C. R. I., “Trailing edge bluntness noise reduction using porous treatments,” *Journal of Sound and Vibration*, Vol. 474, 2020, p. 115257. https://doi.org/https://doi.org/10.1016/j.jsv.2020.115257.

[43] Ali, S. A. S., Azarpeyvand, M., and da Silva, C. R. I., “Experimental study of porous treatment for aerodynamic and aeroacoustic purposes,” *23rd AIAA/CEAS Aeroacoustics Conference*, American Institute of Aeronautics and Astronautics Inc.(AIAA), 2017, pp. AIAA–2017. https://doi.org/https://doi.org/10.2514/6.2017-3358.

[44] Showkat Ali, S. A., Azarpeyvand, M., Szőke, M., and Ilário da Silva, C. R., “Boundary layer flow interaction with a permeable wall,” *Physics of Fluids*, Vol. 30, No. 8, 2018, p. 085111. https://doi.org/https://doi.org/10.1063/1.5043276.

[45] Bowen, L., Celik, A., Zhou, B., Westin, M. F., and Azarpeyvand, M., “The effect of leading edge porosity on airfoil turbulence interaction noise,” *The Journal of the Acoustical Society of America*, Vol. 152, No. 3, 2022, pp. 1437–1448. https://doi.org/10.1121/10.0013703.

[46] Ai, Q., Kamliya Jawahar, H., and Azarpeyvand, M., “Experimental investigation of aerodynamic performance of airfoils fitted with morphing trailing edges,” *54th AIAA aerospace sciences meeting*, 2016, p. 1563. https://doi.org/https://doi.org/10.1016/j.renene.2018.04.066.

[47] Jawahar, H. K., Ai, Q., and Azarpeyvand, M., "Experimental and numerical investigation of aerodynamic performance for airfoils with morphed trailing edges," *Renewable Energy*, Vol. 127, 2018, pp. 355–367. https://doi.org/https://doi.org/10.1016/j.renene.2018.04.066.

[48] Kamliya Jawahar, H., Showkat Ali, S. A., and Azarpeyvand, M., "Aeroacoustic characteristics of slat finlets," *Physics of Fluids*, Vol. 33, No. 9, 2021, p. 097102. https://doi.org/https://doi.org/10.1063/5.0061367.

[49] Gstrein, F., Zang, B., and Azarpeyvand, M., "Trailing-edge noise reduction through finlet-induced turbulence," *Journal of Fluid Mechanics*, Vol. 959, 2023, p. A24. https://doi.org/10.1017/jfm.2023.33.

[50] Liu, X., Kamliya Jawahar, H., Azarpeyvand, M., and Theunissen, R., "Aerodynamic performance and wake development of airfoils with serrated trailing-edges," *AIAA Journal*, Vol. 55, No. 11, 2017, pp. 3669–3680. https://doi.org/https://doi.org/10.2514/1.J055817.

[51] Kamliya Jawahar, H., Showkat Ali, S. A., and Azarpeyvand, M., "Serrated slat cusp for high-lift device noise reduction," *Physics of Fluids*, Vol. 33, No. 1, 2021, p. 015107. https://doi.org/https://doi.org/10.1063/5.0035178.

[52] Mayer, Y. D., Lyu, B., Jawahar, H. K., and Azarpeyvand, M., "A semi-analytical noise prediction model for airfoils with serrated trailing edges," *Renewable Energy*, Vol. 143, 2019, pp. 679–691. https://doi.org/https://doi.org/10.1016/j.renene.2019.04.132.

[53] Celik, A., Mayer, Y. D., and Azarpeyvand, M., "On the aeroacoustic characterization of a robust trailing-edge serration," *Physics of Fluids*, Vol. 33, No. 7, 2021, p. 075120. https://doi.org/10.1063/5.0054767.

[54] Liu, Y., Liu, P., Guo, H., Hu, T., and Zhang, J., "Experimental Study of Far-Field Aerodynamic Noise Characteristics of Serrated Slat," *Journal of Aerospace Engineering*, Vol. 36, No. 1, 2023, p. 04022104. https://doi.org/10.1061/(ASCE)AS.1943-5525.0001509.

[55] "Ultra High aspect ratio wing advanced research and designs," https://cordis.europa.eu/project/id/886552, Mar. 2023. https://doi.org/10.3030/886552, accessed: 2024-1-28.

[56] Mayer, Y., Kamliya Jawahar, H., Szoke, M., and Azarpeyvand, M., "Design of an aeroacoustic wind tunnel facility at the university of bristol," *2018 AIAA/CEAS Aeroacoustics Conference*, 2018, p. 3138. https://doi.org/https://doi.org/10.2514/6.2018-3138.

[57] Mayer, Y. D., Jawahar, H. K., Szőke, M., Ali, S. A. S., and Azarpeyvand, M., "Design and performance of an aeroacoustic wind tunnel facility at the University of Bristol," *Applied Acoustics*, Vol. 155, 2019, pp. 358–370. https://doi.org/https://doi.org/10.1016/j.apacoust.2019.06.005.

[58] Mish, P. F., "An Experimental Investigation of Unsteady Surface Pressure on Single and Multiple Airfoils," *Ph.D. Thesis, Virginia Tech*, 2003.

[59] Jawahar, H. K., Ali, S. A. S., Azarpeyvand, M., and da Silva, C. R. I., "Aerodynamic and aeroacoustic performance of high-lift airfoil fitted with slat cove fillers," *Journal of Sound and Vibration*, Vol. 479, 2020, p. 115347. https://doi.org/https://doi.org/10.1016/j.jsv.2020.115347.

[60] Manoha, E., and Pott-Pollenske, M., "LEISA2: an experimental database for the validation of numerical predictions of slat unsteady flow and noise," *21st AIAA/CEAS Aeroacoustics Conference*, 2015, p. 3137. https://doi.org/https://doi.org/10.2514/6.2015-3137.

[61] Jawahar, H. K., Ali, S. A. S., Azarpeyvand, M., and da Silva, C. R. I., "Aeroacoustic performance of high-lift airfoil with slat cove fillers," *25th AIAA/CEAS Aeroacoustics Conference*, 2019. https://doi.org/https://doi.org/10.2514/6.2019-2440.

[62] Kamliya Jawahar, H., Meloni, S., Camussi, R., and Azarpeyvand, M., "Intermittent and stochastic characteristics of slat tones," *Physics of Fluids*, Vol. 33, No. 2, 2021, p. 025120. https://doi.org/https://doi.org/10.1063/5.0033827.